Research Article

SOHAG JOURNAL OF SCIENCES

https://doi.org/10.21608/sjsci.2025.338797.1237

Influence of oxygen flow rates on the optoelectronic properties SnO_2 thin films

M. A. Awad[1,*], Eman R. Abaza[1], Essam R. Shaaban[2]

[1] *Physics Department, Faculty of Science, Sohag University, 82524 Sohag, Egypt*
[2] *Physics Department, Faculty of Science, Al-Azhar University, Assiut 71542, Egypt*
[*]*Email: arwamadeha@yahoo.com*

Received: 24th November 2024, **Revised:** 1st January 2025, **Accepted:** 8th January 2025
Published online: 28th February 2025

Abstract: SnO_2 thin films were prepared by thermal chemical vapor deposition technique. The furnace temperature, deposition time and Ar flow rate were adjusted at 350ºC, 90 min and 300 sccm, respectively, whereas oxygen flow rates were varied according to preparation condition (100,150 and 200 sccm). The influence of oxygen flow rate on crystal structure, structural parameters, volumetric density, unit cell volume and electrons distribution density were deduced from the output of Rietveld refinement using Fullprof software. It was found that the crystallites size from X-ray diffraction showed synchronization with particle size from scanning electron microscopy analysis. The optical constants are greatly influenced by oxygen flow rate, where both transparency (55%-79%) and optical band gap (4.03- 4.18 eV) were increased with oxygen flow rate unlike that existed in refractive index and extinction coefficient. The catalytic performance of SnO_2 thin films was tested by the decomposition of methylene blue (MB) under UV irradiation. It was found that, the degradation rate of MB is not limited to the presence of Sn_3O_4 mixed phase, where small crystallites allowed small migration length of the photoinduced electrons and holes, and this enhanced the catalytic performance. The degradation efficiency after illumination for 360 min of thin films prepared at oxygen flow rates of 100, 150 and 200 sccm were 87 %, 90% and 92%, respectively.
Keywords: SnO_2 thin; Rietveld refinement; SEM; optical constants; methylene blue.

1. Introduction

Water pollution is a growing global crisis that directly affects health, economic development and food security. The task of water plants is focused on injecting chlorine to break up inorganic compounds and then removing while the organic compounds remain stuck, which pose a great danger to human health. Photolysis is one of the most important techniques for purifying water from organic compounds in the presence of light catalysts [1]. Metal oxides such as ZnO [2], TiO_2 [3], CdS [4] have been effectively used as water purification photocatalysts. As a prominent semiconductor, SnO_2 belongs to the family of metal oxides that achieve both high electrical conductivity and high visible transparency [5]. The interest in the preparation and characterization of SnO_2 thin films is not accidental but the many advantages made it rich material for many applications such as gas sensor [6], biomedical and electrochemical applications [7], and as transparent conductive oxide (TCO) [8]. Despite the lower electrical conductivity of SnO_2 thin compared to indium-tin-oxide (ITO), the highest adhesion and scratch resistance [9] enables their use in high temperature applications [10]. Few reports focused on the catalytic performance of SnO_2 due to large optical band gap and fast recombination of electrons- holes [11, 12]. The creation of native defects in SnO_2 during synthesis is one of methods to improve the catalytic performance and obviate the use of foreign elements in the composition [12]. The mixed valence state of SnO_2 provide extraordinary ability for photocatalysis [13], and charge storage applications [14]. There are two stable phases of stannic oxide, SnO_2 and SnO that are frequently mentioned for industrial applications [15]. Sn_3O_4 is the non-stoichiometric phase of SnO_2 exhibited lately the researcher interest due to of its invaluable catalytic and electrochemical performance [16]. Unfortunately, the recombination of charge caries restrict the usage of Sn_3O_4 in its pure phase in photocatalysis applications [15]. This is what stimulated the researchers to prepare mixed phase containing Sn_3O_4. Yang et al. [17] concluded that the Schottky junctions between Sn/Sn_3O_{4-x} enhanced charge separation, hence the catalytic performance. Yu et all. [18] found that the planar heterostructure of rGO and Sn_3O_4 nanosheets enhanced the separation of electron-hole pairs. Romeiro proved that the ternary $rGO\text{-}Sn_3O_4/SnO_2$ heterostructure exhibited twice performance for H_2 production compared to Sn_3O_4.

Two main methods are used to prepare Sn_3O_4, the carbothermal and solid states method [19, 20], that involve either heating SnO_2 in carbon atmosphere or annealing SnO thus to entail the required phase.

The present study aimed to synthesize SnO_2 – Sn_3O_4 at different oxygen flow rate (100,150 and 200 sccm) and low synthesis temperature (350ºC) using thermal chemical vapor deposition technique (TCVD). A detailed synthetic study was carried out in order to find out the effect of oxygen flow rate on structural, density, volume and electron distribution density of the prepared thin films. According to our knowledge, the

preparation of mixed phase of SnO_2 - Sn_3O_4 using TCVD technique and their application for water purification is not reported yet.

2. Materials and methods

Thin films of SnO_2 - Sn_3O_4 were prepared from Tin (II) chloride dihydrate ($SnCl_4.2H_2O$) at different oxygen flow rates of 100, 150 and 200 sccm using thermal chemical vapor deposition technique (TCVD). First $SnCl_4.2H_2O$ was placed in corundum boat in the center of tubular furnace at temperature of 350ºC, where Ar gas was regulated to flow with flow rate of 300 sccm from the start of the experiment. The Ar and O_2 flows were controlled using mass flow controllers (D07 series Sevenstar) which are connected to flow readout box (D08-4F, sevenstar electronics.com). The ultrasonically cleaned glass and Si substrates were previously aligned in the tubular furnace stating from the boat position along the tube furnace in which the temperature is gradually increased with heating rate of 10º/min. At the end of the experiment, the oven is gradually cooled with the same heating rate**,** where the prepared samples were taken from the furnace for characterization. As a reminder of this work, the samples prepared at 100, 150 and 200 sccm are refer ed as S0, S01 and S02, respectively.

Bruker D8-Advanced X-ray diffractometer with CuK_α (1.54060 Å) was used to investigate the crystal structure of the prepared thin films. The surface morphology and composition stoichiometry were investigated using SEM and EDAX (JEOL, Japan). The optical parameters are deduced by measuring transmission, reflection and absorbance using spectrophotometer (PEAK, model C-7200) where the thicknesses of the prepared thin films are determined using profilometer. The electrical resistivity (ρ) is measured using the conventional two-terminal configuration.

The ability of SnO_2 thin films to degrade wastewater was examined by the decomposition of methylene blue (MB)($C_{16}H_{18}ClN_3S.xH_2O$), where thin films of 2 × 1.5 cm^2 are located in small beaker containing 10 ml of MB dye solution with concentration of 0.003 g/L. A UV light lamp model Germicidal UV-C, G13T8, Japan, with wavelength peak at 254 nm was employed for illumination. The absorption of MB was measured by the spectrophotometer after each period of illumination time in the range 200-800 nm. The degradation rate (C/C_o) of MB was evaluated at the maximum absorption of methylene blue (~660 nm).

3. Results and Discussion

3.1. Structural analysis, Rietveld refinement and crystallites size.

The structural analysis of thin films prepared at different oxygen flow rates of 100, 150 and 200 sccm is depicted in Fig. 1. By comparing the diffracted peak with database, it is discerned the perfectly matching with COD 2104754 of tetragonal SnO_2 phase. Only the peak at $2\theta = 31.7^o$ is defined to match with the plane $(\bar{2}10)$ of triclinic crystal structure of Sn_3O_4 (JCPDS No. 16-0737) [18]. It was previously reported that the diffraction peaks of Sn_3O_4 phase is completely eliminated and totally transferred to tetragonal phase of SnO_2 at 500ºC [21]. As it clear, the crystallization efficiency first increased (Fig. 1b) then decreased (Fig. 1c) with increasing oxygen flow rate. The first increase is resulted from the increment of population density of both Sn and O_2 atoms in the reaction zone that increased nucleation and growth rates [22]. The over ratio of oxygen atmosphere (200 sccm) deteriorated the crystal quality as a result of adatoms scramble in the reaction zone that increased stresses and scattering effect, and produced out of plane interference in what is known diffraction halo [23]. Similar results are reported elsewhere [3, 24]. On the other hand, the portion of the Sn_3O_4 phase is decreased due to the increment of oxygen flow rate.

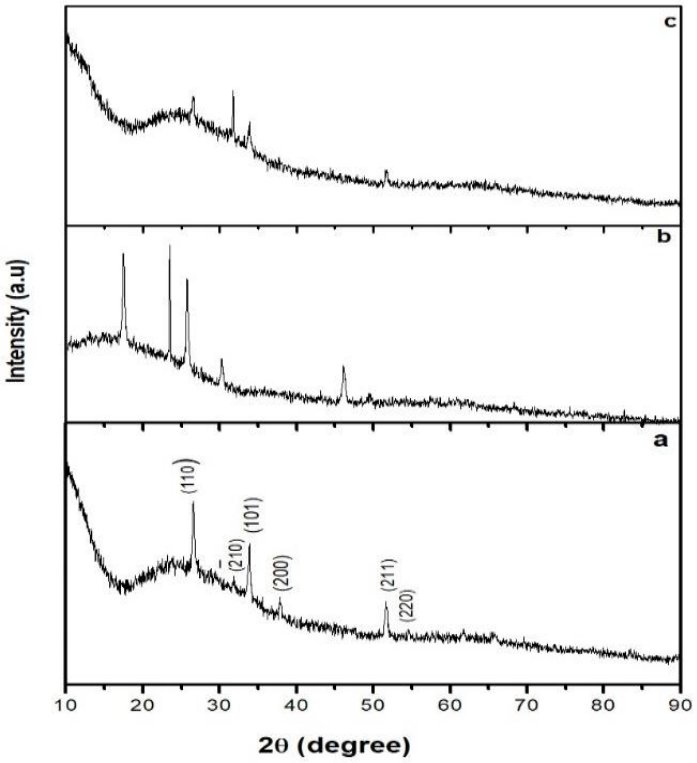

Figure 1: XRD of SnO_2 thin films at different oxygen flow rates of (a) 100 sccm, (b) 150 sccm and (c) 200 sccm.

The Rietveld refinement using fullprof-suite software confirmed the tetragonal symmetry of SnO_2 with space group of P 42/m nm and lattice parameters (Table 1) that are close to the values reported elsewhere [25]. The pseudo-Voigt is the function used to refine the peak shape and the FWHM of the diffracted peaks. The refined XRD (Fig. 2) after excluding the $(\bar{2}10)$ plane of anorthic Sn_3O_4 clarified the good fitting between experimental (red line) and theoretical data (black line). The refined data is used to determine the bond length and bond angle using vesta-software.

Fig. 3 shows that both bond lengths and bond angles are changed with increasing oxygen flow rate. These changes are in order to lower the internal energy in nonlinear-degenerate molecules in what is known Jahn Teller distortion [26]**.** Fig. 4 shows the consequences of Jahn Teller distortion on changing the unit cell volume which behaved oppositely with volumetric density. The relatively low density and large unit cell volume

for S01 is related to the prominent mixed phase of Sn_3O_4 that have larger lattice parameters (a = 4.85 Å, b = 5.87 Å and c = 8.20 Å) [27] compared to the SnO_2 (see Table 1).

Table 1: The refined parameter of SnO_2 thin films at different oxygen flow rates

Oxygen flow rate (sccm)	Crystal system	Space group	Lattice parameters (Å)	Volume (Å^3)	χ^2	Density (g/cm^3)
100	Tetragonal	P 42/m n m (136)	a = b = 4.7602, c = 3.2014	72.5406	0.99	6.713
150	Tetragonal	P 42/m n m (136)	a = b = 4.7609, c = 3.2010	72.5519	1.25	6.381
200	Tetragonal	P 42/m n m (136)	a = b = 4.7531, c = 3.1856	71.9678	1.06	6.955

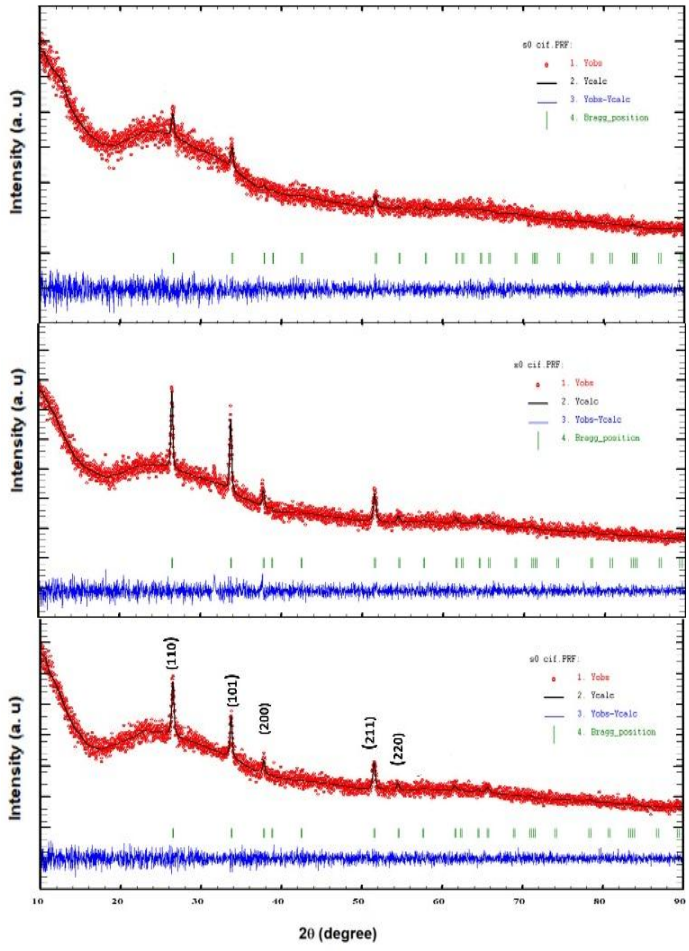

Figure 2: The refined XRD at different oxygen flow rates of (a) 100 sccm, (b) 150 sccm and (c) 200 sccm.

The G Fourier program is used to plot the electron distribution density (Fig. 5) within the unit cell, where electrons density increased with increasing oxygen flow rate. This is related to the replacement of oxygen by Cl which have the higher valency.

The crystallite size using modified Sherrer equation [28] showed synchronization with crystalline quality (Table 2). The influence of oxygen flow rate on particle size of SnO_2 is reported previously [29, 30], where increasing oxygen flow tends to decrease the particles size.

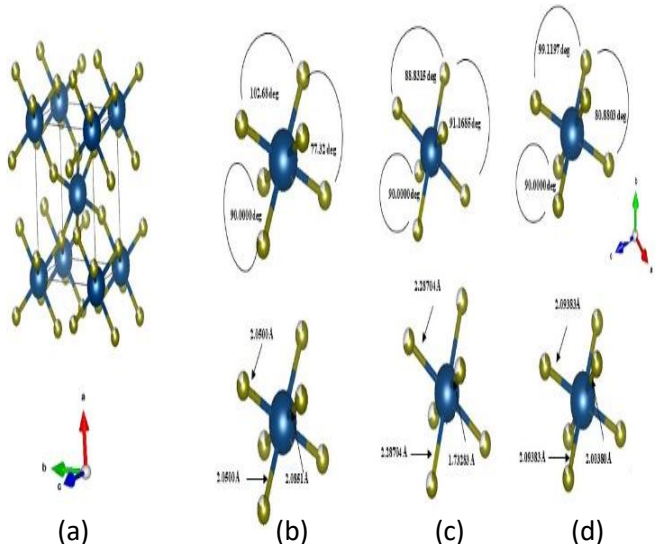

Figure 3: The changes in bond length and bond angle with oxygen flow rate.

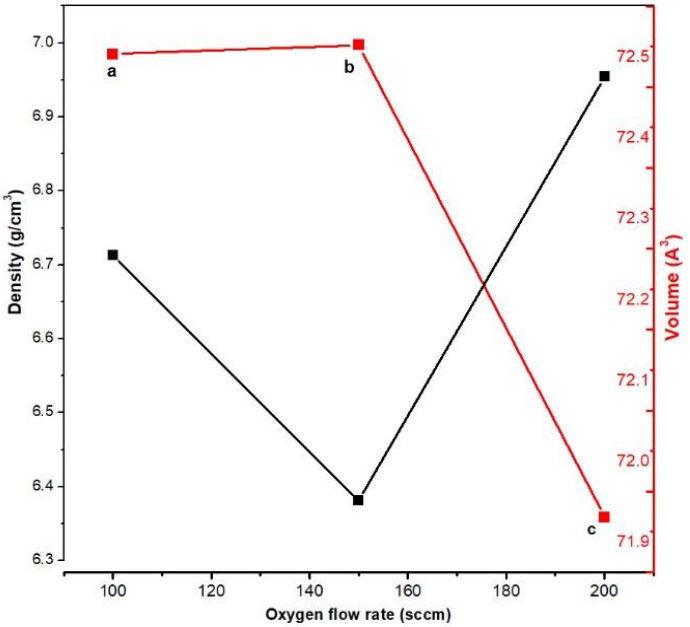

Figure 4: The variation of unit cell volume and density with oxygen flow rate of (a) 100 sccm, (b) 150 sccm and (c) 200 sccm.

3.2. Morphological and compositional analysis

The surface morphology of the thin films (Fig. 6) revealed the formation of similar rice morphology (Fig. 6a) that is

transferred into the nanoparticles form when oxygen flow rate increased to 150 sccm (Fig. **6b**). These nanoparticles became more condensed and coalceded with increasing oxygen flow rate to 200 sccm (Fig. **6c**). The presence of Cl atoms as an impurity in S02 allowed their segregation through grain boundaries and accordingly decreased grain growth [24]. Although the calculated crystallites size from XRD is lower than particles size from SEM image, both showed plateau like behavior [31]. The growth mechanism of nanoparticles is summarized as follows: increasing the furnace temperature allowed Sn, O and Cl species to transfer by carrier gas to impinge on the Si and glass substrates. Where they slide to a certain distance before finding their stationary position. This is governed by several factors such as the activation energy of the condensed species, temperature and the sticking coefficient of adatoms with each other and with the substrates [32]. Increasing deposition rate to 200 sccm at low substrates temperatures (350ºC) reduced the reactivity between Sn and O atoms and favored the Sn and Cl bonds.

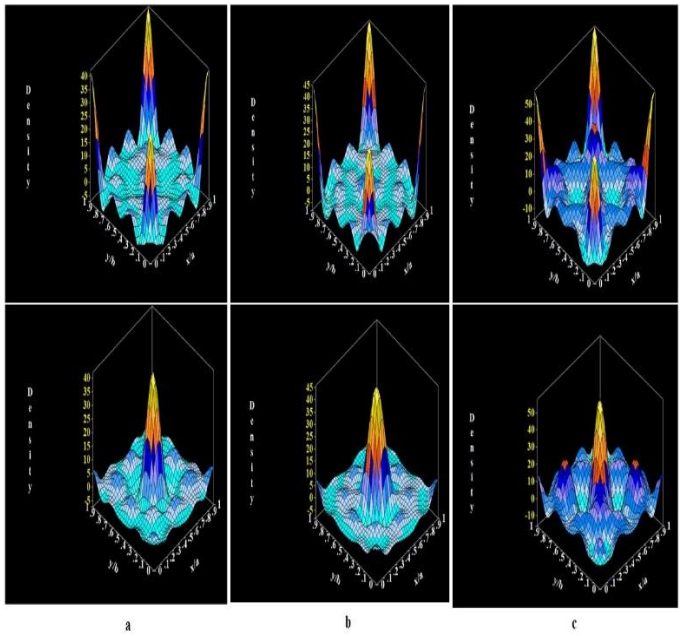

Figure 5: Electron distribution of SnO_2 using different oxygen flow rates of (a) 100 sccm, (b) 150 sccm and (c) 200 sccm.

Table 2: Crystallite size (D), chemical composition, optical band gap (E_g), static dielectric constant (ε_0), resistivity(ρ), sheet resistance (R_{sh}) anf FOM of SnO_2 thin films at different oxygen flow rate.

Oxygen flow rate (sccm)	D (nm)	Sn	O	Cl	E_g (eV)	ε_0	ρ (ohm.cm) × 10^{-1}	R_{sh} ×10^4 (ohm/square)	FOM × 10^{-7} (ohm^{-1})
100	27.7	39.02	60.98		4.03	6.11	3.6	1.8	1.4
150	32.5	38.47	61.53		4.08	5.95	4.4	1.83	9.9
200	20.5	40.24	44.13	15.63	4.18	5.64	20.2	7	13

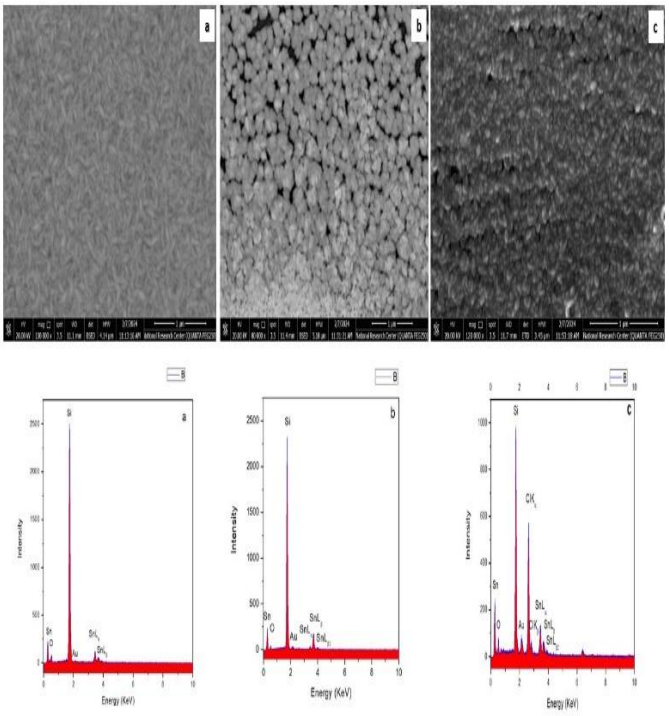

Figure 6: SEM and EDAX analysis of SnO_2 at different oxygen flow rates of (a) 100 sccm, (b) 150 sccm and (c) 200 sccm.

The elemental composition using EDAX analysis (Fig. **6** and Table **2**) confirmed the presence of both Sn and O atoms. The prominent of Cl signal at oxygen flow rate of 200 sccm although their absence in XRD results (Fig. **1**) indicated their location in interstitial position within the crystal lattice as well as in the amorphous phase. The disappearance of Cl peaks in S0 and S01 didn't negate their presence, but this may mean the signal coming from chlorine was weak. From Table **2**, it is discerned that oxygen varied irregularly with oxygen flow rate. The deviation from the stoichiometry suggested the presence of Sn_i as well as O_v.

3.3. Optical and electrical discussion

The behavior of light beam when falling on the thin films in the wavelength range (190-1100 nm) is represented in Fig. **7**. The large transmission window of all thin films is correlated with the disparity of atomic weight of both Sn (118.710) and oxygen (15.999) atoms that decreased the columbic bond [23, 33]. The average transparency of S0 (Fig. **7a**) in the wavelength range (400 - 800 nm) is not very large (55%) as reported elsewhere [34]. The reason relied on photons' scattering by oxygen vacancies that form shallow levels within the band gap [35]. The increase in transparency with increasing oxygen flow rate (67% for S01 and 79% for S02) is related to the gradual elimination of oxygen vacancies [34]. Worth noting the average transparency of S02 is close to the values reported elsewhere [31]. The reflectivity behaved oppositely, where there is decrease with oxygen flow rates.

The optical band gap (E_g) of thin films at different oxygen flow rate is calculated using the direct allowed transition of Tauc relation given by,

$$(\alpha h\nu)^2 = \beta(h\nu - E_g) \quad (1)$$

where β is constant, $h\nu$ is the photon energy and α is the absorption coefficient. The E_g values increased with oxygen flow rate (Fig. 8). The increase in E_g values is related to oxygen vacancies elimination by either oxygen incorporation or by the unintentional doping of Cl atoms that caused oxygen sub-stoichiometry by substitution of their positions. The increase in E_g values with oxygen flow rate is consistent with previous reports [31] and is contradicted with others [36].

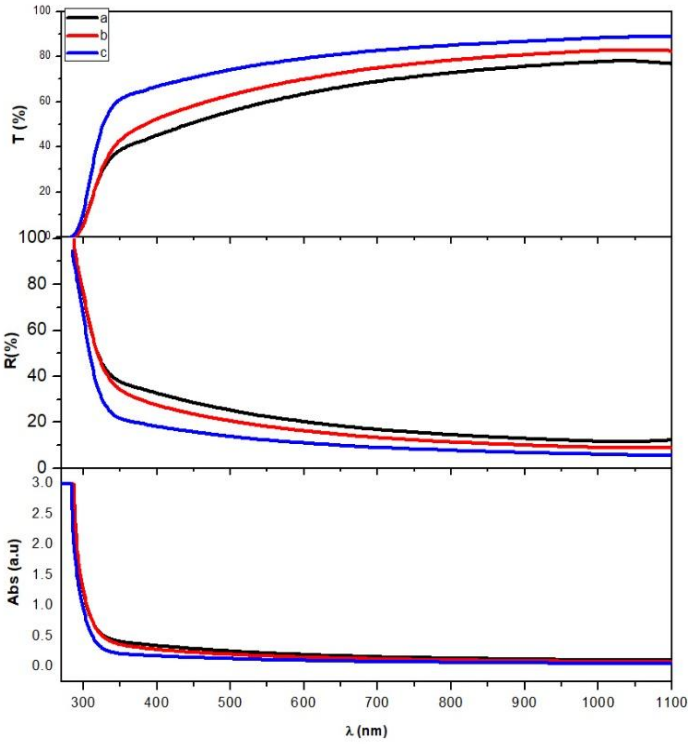

Figure 7: The optical behavior of SnO_2 thin films at different oxygen flow rates of (a) 100 sccm, (b) 150 sccm and (c) 200 sccm.

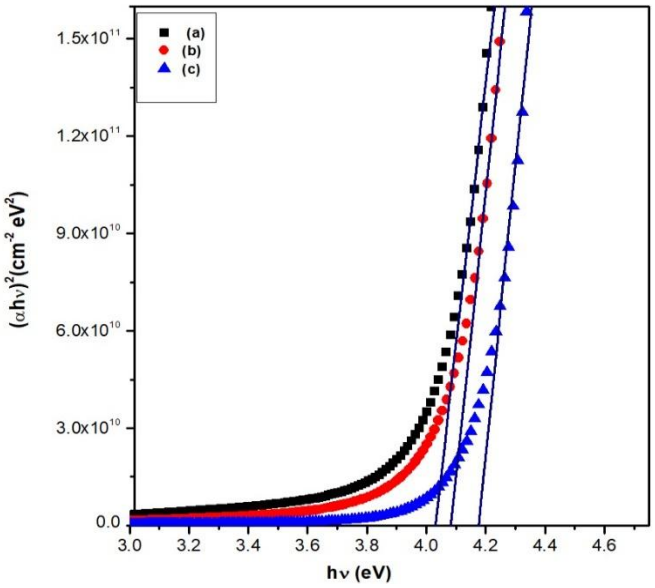

Figure 8: The optical band gap of SnO_2 thin films at different oxygen flow rates of (a) 100 sccm, (b) 150 sccm and (c) 200 sccm.

The static dielectric constant $(\mathcal{E}_0)$ of SnO_2 thin films at different oxygen flow rates is calculated using the relation [37],

$$\mathcal{E}_0 = 18.52 - 3.08\, E_g \quad (2)$$

where E_g is the optical band gap. Table 2 summarized the value of $\mathcal{E}_0$, where they are increased with increasing donor density and decreased with increasing the optical band gap.

The plot of optical parameters (refractive index, n, and extinction coefficient, k) with wavelength is presented in Fig. 9. It is clear that, both refractive index and extinction coefficient decreased with increasing oxygen flow rate [35], which is correlated to the decrease of absorption centers and to the increase of the optical band gap.

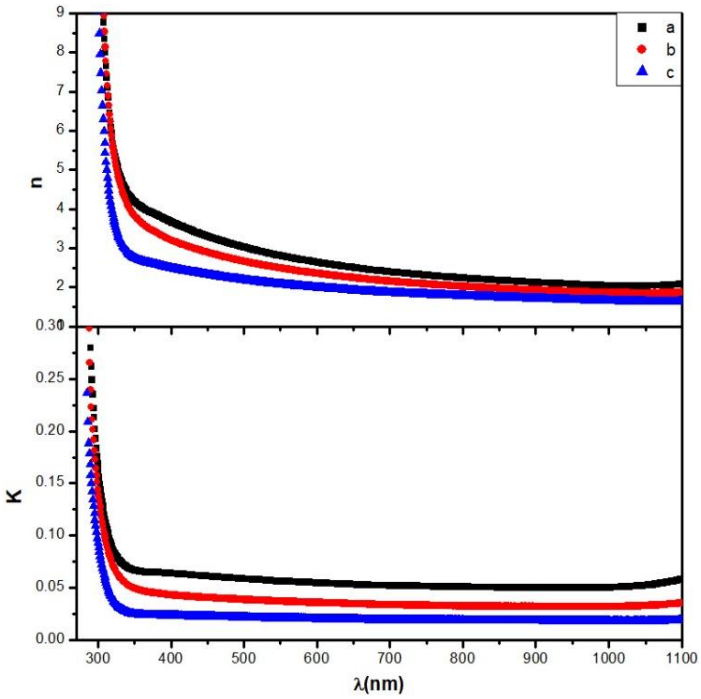

Figure 9: The refractive index (n) and extinction coefficient (k) of SnO_2 thin films at different oxygen flow rates of (a) 100 sccm, (b) 150 sccm and (c) 200 sccm.

Measurement of resistivity at room temperature (ρ_{room}) shows increase with oxygen flow rate (Table 2). The reasons ascribed to the gradual decline of oxygen vacancies that decreased free carrier concentration [30], as well as charge carriers scattering due to amorphous phase and grain-boundary potential barriers [7]. Worth noting, the values of resistivity and sheet resistance are higher than the values reported elsewhere [38] and lower than others [39].

Fig. 10 explain the variation of resistivity of SnO_2 thin films with temperature in the temperature range from 300 to 573 K. While there is smooth descent in resistivity for the thin films prepared at 100 sccm (Fig.10a), the situation is different when oxygen flow rate has been increased to 150 sccm (Fig.10b). Where the decrease is very slow below 360 K and start to become significant after that. This is related to the promotion of electrons from different localized states [40] of SnO_2. The huge decrease in electrical resistivity of S02 confirmed the location

of Cl atoms in oxygen position in the crystal lattice [41], where the high temperature activated their transition into the conduction band.

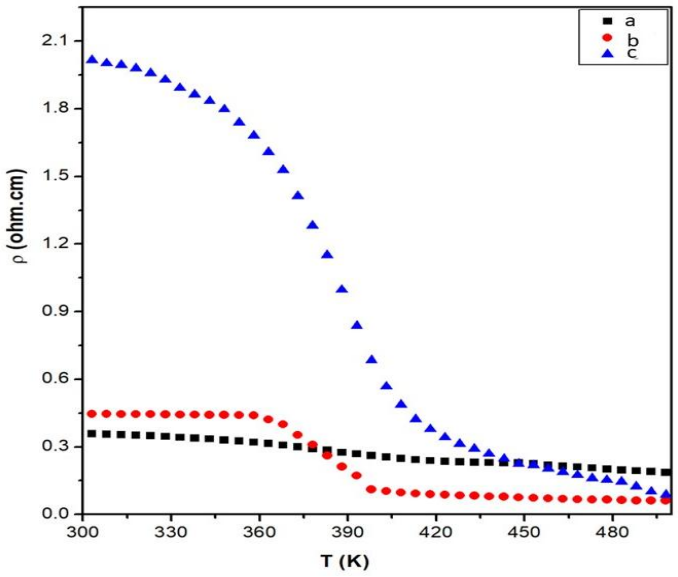

Figure 10: The resistivity of SnO_2 thin films with temperature at different oxygen flow rates of (a) 100 sccm, (b) 150 sccm and (c) 200 sccm.

To evaluate the extent of using SnO_2 thin films in TCO applications, the Haacke's relation is used to calculate the Figure of merit (FOM) [42] according to,

$$FOM = \frac{T_{av}{}^{10}}{R_{sh}} \quad (3)$$

where $T_{av}{}^{10}$ is the average transparency and R_{sh} is the sheet resistance. From which, the highest Figure of merit is recorded for the thin films prepared at oxygen flow rate of 200 sccm (see Table 2), that doesn't fit the industrial requirement.

3.4. The photocatalytic activity of SnO_2 thin films

The catalytic performance of SnO_2 thin films was tested by the decomposition of MB. Fig. 11 shows the changes in absorbance of MB dye under different illumination times. The degradation rate was evaluated at the maximum absorption of methylene blue (~660 nm). Clearly, the absorbance of MB decreased with increasing illumination time as a result of MB decomposition. The amount of degradation after illumination for 360 min are 87 %, 90% and 92% for S0, S01 and S02, respectively.

To find out the effect of oxygen flow rates on the degradation rate of SnO_2 photocatalysts thin films, Fig. 12 explains the behavior. Clearly, the degradation rate is slightly increased for S01 compared to S0 due to the presence of Sn_3O_4 phase that facilitated charge transfer [43]. The degradation efficiency of S02 is greatly increased despite the high optical band gap. The reason relied on the small particles size that allowed small migration length of the photoinduced electrons and holes, and this enhanced the catalytic performance through the separation of electron-hole pairs.

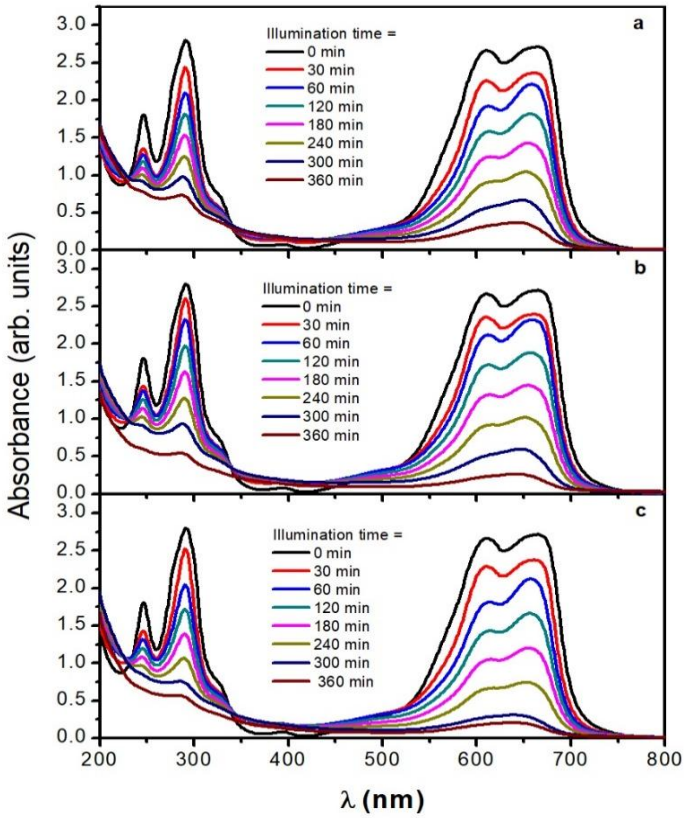

Figure 11: The changes in absorbance of SnO_2 thin films, prepared at different oxygen flow rates of (a) 100 sccm, (b) 150 sccm and (c) 200 sccm with illumination time.

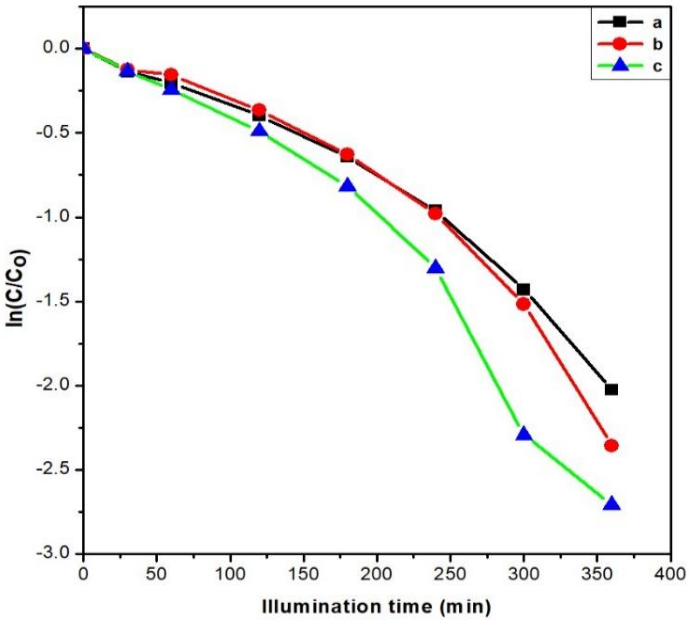

Figure 12: The degradation rate of SnO_2 thin films at different oxygen flow rates (100 (a), 150 (b) and 200 (c).

The steps to decompose MB under UV illumination can be summarized as follows,

- $SnO_2 + h\nu \rightarrow SnO_2(e^-_{CB} + h^+_{VB})$
- $O_2(ads) + e^-_{CB} \rightarrow O_2^-$

- $H_2O + h^+_{VB} \rightarrow OH^\bullet + H^+$
- $2e^-_{CB} + 2H^+ + O_2 \rightarrow H_2O_2$
- $H_2O_2 + e^-_{CB} \rightarrow OH^\bullet + OH^-$
- $h^+_{VB} + H_2O \rightarrow H^+ + OH^\bullet$
- $OH^\bullet + \ Organicdye \ \rightarrow CO_2 + H_2O$

From the aforementioned equations it is concluded that, the catalytic performance initiates once the UV light fall on SnO_2 thin films, where electrons are exited from the valence band to conduction band of SnO_2. The presence of Sn_3O_4 phase allowed these electrons to be injected into its conduction band with retaining the holes in their position [44]. The function of electrons is to reduce the adsorbed oxygen to superoxide ions O_2^-, while holes are reacted with hydroxyl group to produce hydroxyl radicals $OH^\bullet$.

From the foregoing discussions it is concluded that, the catalytic performance of SnO_2 thin films is not limited to the presence of Sn_3O_4 as a mixed phase, but small particles size has a big role for increasing the catalytic performance.

4. Conclusion

SnO_2 thin films was successfully prepared at different oxygen flow rates using thermal chemical vapor deposition technique. A detailed structure study is carried out in order to see the influence of oxygen flow rate on the structural parameter and crystal structure of SnO_2. It was found that both optical and electrical properties are greatly affected by oxygen flow rate. All the SnO_2 thin films have excellent photocatalytic performance. The catalytic performance of SnO_2 thin films is not limited to the presence of Sn_3O_4 as a mixed phase, but small particles size has a big role in increasing the catalytic performance.

CRediT authorship contribution statement:

Conceptualization has been done by M.A.A, E.R.A. and E.R.S.; methodology has been carried out by M.A.A and E.R.A.; software has been carried out by M.A.A.; validation has been done by M.A.A, E.R.A. and E.R.S; resources has been carried out by M.A.A.; data curation has been carried out by M.A.A. and E.R.A.; writing—original draft preparation has been carried out by M.A.A. and E.R.A.; writing—review and editing, has been carried out by M.A.A. and E.R.A.; visualization has been carried out by M.A.A. and E.R.A.; supervision has been carried out by M.A.A. and E.R.S.; All authors have read and agreed to the published version of the manuscript.

Data availability statement

The data are available upon request from the corresponding author.

Declaration of competing interest

The authors declares that there is no conflict of interest.

Acknowledgments

I would like to thank my student Abdelrahman M. Rayan for helping me to learn the basics of Rietveld refinement.

References

[1] S. B. Ameur, A. Barhoumi, H. B. Hadjltaief, R. Mimouni, B. Duponchel, G. Leroy, M. Amlouk, H. Guermazi, *Materials Science in Semiconductor Processing*, 61 (2017) 17.
[2] M. A. Awad, E. M. M. Ibrahim, A. M. Ahmed, *The European Physical Journal Applied Physics*, 72 (2015) 30303.
[3] M.A. Awad, M. Raaif, Applied Physics A, 124 (2018) 388.
[4] Q. Sun, N. Wang, J. Yu, J.C. Yu, *Advanced Materials*, 30 (2018) 1804368.
[5] P.P. Edwards, A. Porch, M.O. Jones, D.V. Morgan, R.M. Perks, *Dalton Transactions*, Issue 19 (2004) 2995-3002.
[6] Y. Masuda, *Sensors & Actuators: B. Chemical*, 364 (2022) 131876.
[7] T. R. Giraldi, M. T. Escote, M. I. B. Bernardi, V. Bouquet, E. R. Leite, E. Longo, and J. A. Varela, *Journal of Electro-ceramics*, 13 (2004) 159.
[8] X. Li, T. Gessert, C. DeHart, T.M. Barnes, H. Moutinho, Y. Yan, D.L. Young, M. Young, J.D. Perkins, and T. Coutts, Proc. NCPV Program Review Meeting, Lakewood, CO (2001) 255.
[9] G. Bräuer, J. Szczyrbowski, G. Teschner, *Surface and Coatings Technology*, 94 (1997) 658.
[10] Y. Kong, Y. Li, X. Cui, L. Su, D. Ma, T. Lai, L. Yao, X. Xiao, and Y. Wang, *Nano Materials Science*, 4 (2022) 339.
[11] J. Mazloom, F. E. Ghodsi, H. Golmojdeh, *Journal of Alloys and Compounds*, 639 (2015) 393.
[12] L. G. da Trindade, A. C. B. Rocha, V. Teodoro, V. T. da Silva, A. B. Trench, E. Cordoncillo, M. D. Teodoro, S. M. Tebcherani, E. Longo, and T. M. Mazzo, *Materials Research Bulletin*, 153 (2022) 111914.
[13] S. S. Shabna, S. Sahaya Jude Dhas, C. S. Biju, *Catalysis Communications*, 177 (2023) 106642.
[14] S. Amuthameena, K. Dhayalini, B. Balraj, C. Siva, and N. Senthilkumar, *Inorganic Chemistry Communications*, 131 (2021) 108803.
[15] X. Yu, C. Li, J. Zhang, L. Zhao, J. Pang, and L. Ding, *International Journal of Minerals, Metallurgy and Materials*, 31 (2024) 231.
[16] A. Seko, A. Togo, F. Oba, and I. Tanaka, *Physical Review Letters*, 100 (2008) 045702.
[17] R.-q. Yang, N. Liang, X.-y. Chen, L.-w. Wang, G.-x. Song, Y.-c. Ji, N. Ren, Y.-w. Lü, J. Zhang, and X. Yu, *International Journal of Minerals, Metallurgy and Materials*, 28 (2021) 150.
[18] X. Yu, Z. Zhao, D. Sun, N. Ren, J. Yu, R. Yang, and H. Liu, *Applied Catalysis B: Environmental*, 227 (2018) 470.
[19] L. Zhang, X. Liu, X. Zhang, W. Zhang, J. Ma, Q. Wang, and S. Su, *Journal of Alloys and Compounds*, 961 (2023) 170904.
[20] N. Yuan, X. Zhang, B. Li, T. Chen, and X. Yang, *ACS Applied Nano Materials*, 6 (2023) 9159.
[21] J. Wang, C. Lu, X. Liu, Y. Wang, Z. Zhu, and D. Meng, *Materials & Design*, 115 (2017) 103.
[22] M. A. Awad, A. M. Ahmed, and E. M. M. Ibrahim, *International Journal of New Horizons in Physics*, 2 (2015) 59-61.
[23] M. A. Awad and M. A. Rabia, *Ceramics International*, 49 (2023) 37340.
[24] M. Awad and A. M. Abu-Dief, *Physica Scripta*, 97 (2022) 085811.
[25] F. A. Akgul, C. Gumus, A. O. Er, A. H. Farha, G. Akgul, Y. Ufuktepe, and Z. Liu, *Journal of Alloys and Compounds*, 579 (2013) 50.
[26] H. Ahn and E. Teller, *Proceedings of the Royal Society A*, 161 (1937) 220.
[27] W. Xu, M. Li, X. Chen, J. Zhao, R. Tan, R. Li, J. Li, and W. Song, *Materials Letters*, 120 (2014) 140.
[28] A. Monshi, M. R. Foroughi, and M. R. Monshi, *World Journal of*

Nano Science and Engineering, 2 (2012) 154.
[29] M. Alaf, M. O. Guler, D. Gultekin, M Uysal, A. Alp, H. Akbulut, Vacuum, 83 (2008) 292.
[30] M. Maleki and S. M. Rozati, *Physica Scripta*, 86 (2012) 015801
[31] Y.M. Lu, J. Jiang, C. Xia, B. Kramm, A. Polity, Y.B. He, P. J. Klar, and B. K. Meyer, *Thin Solid Films*, 594 (2015) 270.
[32] J.A Venables, Introduction to Surface and Thin Film Processes, Cambridge University Press, 2000.
[33] W. Vogel, Structure and Properties of Colorless Glasses, In: W. Vogel, (eds) Glass Chemistry. Springer, Berlin, Heidelberg, (1994) ch.7, 123.
[34] Z. Songqing, Z. Yueliang, W. Shufang, Z. Kun, H. Peng, *Rare Metals*, 25 (2006) 693.
[35] M. A. Awad and M. A. Rabia, *Applied Physics A*, 128 (2022) 225.
[36] Y. Tao, B. L. Zhu, Y. Yang, J. Wu, and X. Shi, *Materials Chemistry and Physics*, 250 (2020) 123129.
[37] M. A. Yıldırım, *Optics Communications*, 285 (2012) 1215.
[38] S. Raghunath Reddy, A. K. Mallik, and S. R. Jawalekar, *Bulletin of Materials Science*, 8 (1986) 357.
[39] S.Y. Yoon, B.J. Choi, *Archives of Metallurgy and Materials*, 65 (2020) 1041.
[40] I.-H. Ahn, D. Y. Kim, and S. Lee, *Nanomaterials*, 11 (2021) 585.
[41] Y.Wang, M.Feng, H. Chen, M. Ren, H. Wang, Y. Miao, Y. Chen, Y. Zhao, *Advanced Materials*, 36(2024) 2305849.
[42] G. Haacke, *Journal of Applied Physics*, 47 (1976) 4086.
[43] E. Gribov, E. Koshevoy, A. Kuznetsov, M. Mikhnenko, E. Losev, and M. Lyulyukin, *Materials*, 16 (2023) 7300.
[44] W. Xia, H. Wang, X. Zeng, J. Han, J. Zhu, M. Zhou, and S. Wu, *Cryst. Eng. Comm*, 16 (2014) 6841.